

# Universal quantum dynamics of Bose polarons

Jiří Etrych, Gevorg Martirosyan, Alec Cao,<sup>†</sup> Christopher J. Ho, Zoran Hadzibabic, and Christoph Eigen<sup>\*</sup>  
*Cavendish Laboratory, University of Cambridge, J. J. Thomson Avenue, Cambridge CB3 0HE, United Kingdom*

Predicting the emergent properties of impurities immersed in a quantum bath is a fundamental challenge that can defy quasiparticle treatments. Here, we measure the spectral properties and real-time dynamics of mobile impurities injected into a homogeneous Bose–Einstein condensate, using two Feshbach resonances to tune both the impurity-bath and intrabath interactions. We map out both attractive and repulsive branches of polaron quasiparticles, resolving the repulsive polaron and the molecular state associated with the Feshbach resonance in the strongly interacting regime, and show that the latter also has a many-body character. Our measurements reveal remarkably universal behavior, controlled by the bath density and a single dimensionless interaction parameter; for near-resonant interactions the polarons are no longer well defined, but the universality still holds.

Understanding strongly correlated quantum matter is a fundamental goal of many-body physics. Remarkably, complex systems with many interacting degrees of freedom, from Fermi liquids [1] to superfluids [2], are often amenable to relatively simple quasiparticle descriptions. The polaron, a mobile impurity dressed by the excitations of a medium, is a paradigmatic quasiparticle, originally conceived to describe electrons moving through a crystal [3, 4] and now relevant in many contexts, from condensed matter [5] to surface chemistry [6] and quantum computation [7].

Experiments with neutral ultracold atoms have served as a powerful platform for studying Fermi [8–20] and Bose [21–29] polarons, where impurity atoms are coupled to a spin-polarized Fermi sea or a Bose–Einstein condensate (BEC). Crucially, impurity-bath interactions (characterized by the scattering length  $a$ ) can be tuned to be either attractive or repulsive, and either weak or strong, by exploiting Feshbach resonances [32] associated with a bound state of the impurity and a bath atom. In vacuum, this dimer state (with reduced mass  $m_r$ ) has energy  $E_d = -\hbar^2/(2m_r a^2)$  for  $a > 0$  and becomes unbound on resonance ( $a \rightarrow \infty$ ), while in a medium it may instead connect to the negative-energy attractive polaron at  $a < 0$  [33, 34]. For the Fermi polaron, it is established that the quasiparticle picture holds even in the strongly interacting regime [35, 36], while in the Bose case, where the impurity can dramatically distort the more compressible bath, the validity of a quasiparticle description is an open question [37–39]. Moreover, while a spin-polarized atomic Fermi sea is typically noninteracting, in the case of a BEC, both repulsive intrabath interactions (characterized by the scattering length  $a_b$ ) and three-body Efimov correlations make the problem more intricate [34, 37–47].

Bose polarons in the strongly interacting regime have so far been investigated using harmonically trapped BECs [21, 22, 24–26, 28], with the measurements averaging their properties over an inhomogeneous bath density. Here we realize the textbook scenario of impurities injected into a quasi-uniform BEC, prepared in an optical box trap [49]. We vary  $a$ ,  $a_b$ , and the homogeneous bath density  $n$ , observe consistent impurity energy spectra and real-time dynamics, and study both attractive and repulsive polarons, as well as the molecular state; for the latter, the spectral peak matches the bare dimer energy  $E_d$ , but the full spectrum reveals its many-body character. In all cases, we observe behavior universally set by the dimensionless interaction parameter  $1/(k_n a)$  and the energy  $E_n = \hbar^2 k_n^2 / (4m_r)$ , where  $k_n = (6\pi^2 n)^{1/3}$ .

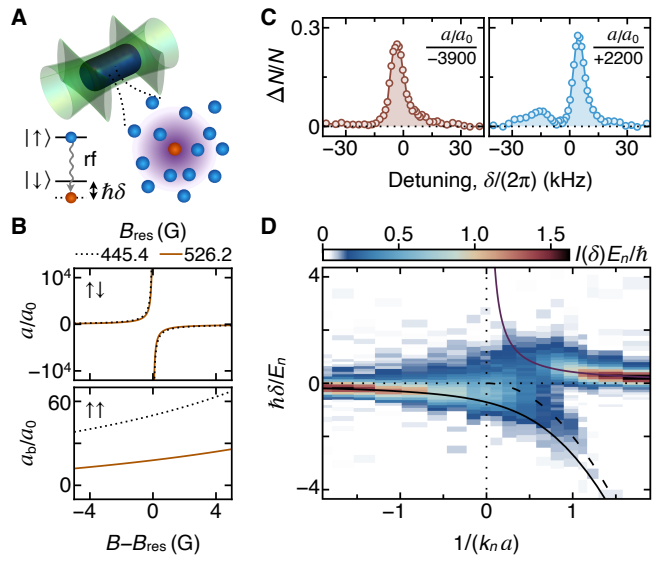


FIG. 1. Bose polarons in a box. (A) Sketch of the box trap and the polaron: an impurity (red,  $|\downarrow\rangle$ ) interacting with a many-body bath (blue,  $|\uparrow\rangle$ ) of homogeneous density  $n$ . Starting with a spin-polarized BEC, we use an rf pulse (detuned by frequency  $\delta/(2\pi)$  from the bare transition) to create a small population of the impurity state. (B) Impurity-bath interactions, characterized by the interstate scattering length  $a$ , are tuned using one of two Feshbach resonances (top), with different values of the intrabath scattering length  $a_b$  (bottom);  $a_0$  is the Bohr radius. (C, D) Overview of the impurity spectrum near  $B_{\text{res}} = 526.2$  G for  $n \approx 12 \mu\text{m}^{-3}$ . (C) Characteristic injection spectra (measured via fractional atom loss  $\Delta N/N$ , see text): for attractive interactions (left), a single spectral feature is observed, while for repulsive interactions (right), the spectrum is bimodal. (D) Injection spectra  $I(\delta)$  across the Feshbach resonance. We express all quantities in dimensionless form, using the density-set momentum scale  $k_n \approx 9 \mu\text{m}^{-1}$  and energy scale  $E_n/\hbar \approx 2\pi \times 10 \text{ kHz}$ . The solid lines show the single-phonon ansatz predictions [33, 48] for the energy of the attractive (black) and repulsive (purple) polaron. The dashed line shows the bare Feshbach dimer energy  $E_d$ .

## Experimental system

Our experiments start with a quasi-pure weakly interacting  $^{39}\text{K}$  BEC, confined in an optical box trap [49–51] and spin-polarized in a hyperfine state denoted  $|\uparrow\rangle$ . A small population of impurities in an adjacent hyperfine state  $|\downarrow\rangle$  can be created using an rf pulse (see Fig. 1A). We either perform injection spectroscopy, measuring the fraction of  $|\downarrow\rangle$  atoms after a pulse of duration  $t_{\text{rf}}$  and varying frequency  $\omega/(2\pi)$ , or interferometry based on two short rf pulses separated by an evolution time  $t$ . We work with two combina-

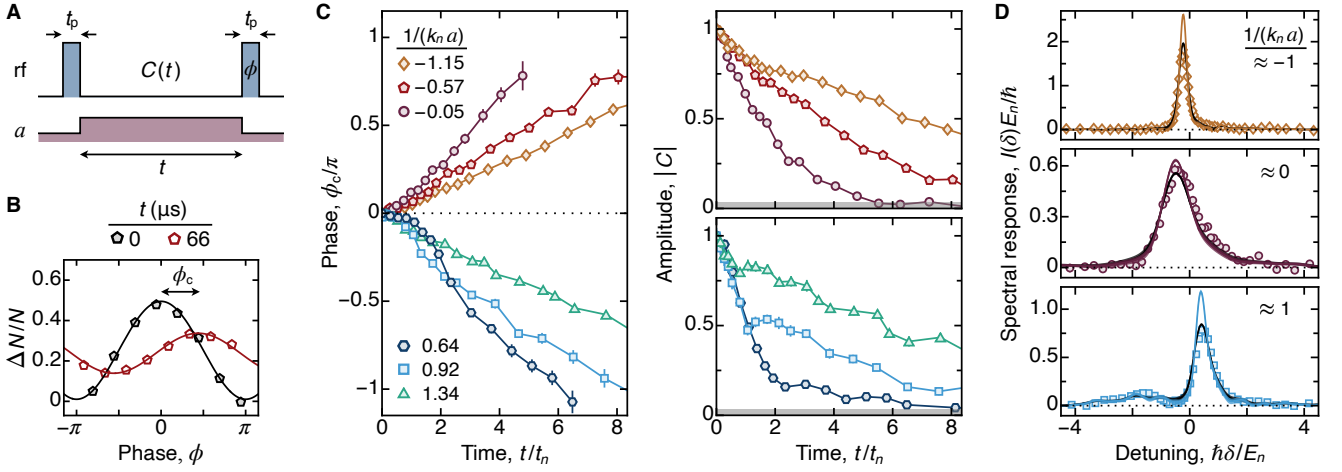


FIG. 2. Interferometric measurement of impurity dynamics. (A) We use two short rf pulses of length  $t_p$  separated by a variable time  $t$  to access the coherence function  $C(t) = |C(t)| \exp[i\phi_c(t)]$ . We perform the pulses at weak interactions and use  $B$ -field quenches to set  $a$  in between. (B) Typical traces of  $\Delta N/N$  versus the phase of the second pulse,  $\phi$ , at  $1/(k_n a) = -0.57$ ;  $C(t)$  is obtained from the contrast and phase shifts using sinusoidal fits (solid lines). (C) Evolution of  $\phi_c(t)$  (left) and  $|C(t)|$  (right) for varying  $a$  at fixed  $n = 12(1)\mu\text{m}^{-3}$  ( $t_n \approx 16\mu\text{s}$ ). The error bars reflect fitting errors and our noise floor for  $|C|$  is  $\approx 3\%$  (shaded band). (D) Comparison of the interferometric and spectroscopic measurements, for three different interaction parameters. We show the Fourier transforms of  $C(t)$  (colored lines), the injection spectra (symbols), and the former numerically broadened to mimic the finite- $t_{\text{rf}}$  broadening of the latter (black lines). The line thickness and error bars reflect measurement errors.

tions of  $|\uparrow\rangle$  and  $|\downarrow\rangle$  states, near two different Feshbach resonances (see Fig. 1B); in the low-field  $|F, m_F\rangle$  basis, we use either  $|\uparrow\rangle = |1, -1\rangle$  and  $|\downarrow\rangle = |1, 0\rangle$  with  $B_{\text{res}} = 526.16(3)\text{G}$ , or  $|\uparrow\rangle = |1, 0\rangle$  and  $|\downarrow\rangle = |1, 1\rangle$  with  $B_{\text{res}} = 445.42(3)\text{G}$  [52, 53]. The two bath states have  $a_b$  values that differ by a factor of  $\approx 3$  near  $B_{\text{res}}$ , and we vary  $n$  in the range  $(3 - 22)\mu\text{m}^{-3}$ , corresponding to  $E_n/\hbar = 2\pi \times (4 - 15)\text{kHz}$  and characteristic time  $t_n = \hbar/E_n = (10 - 40)\mu\text{s}$ . We calibrate  $n$  by measuring the impurity mean-field energy at low  $|a|$  (see [54]).

For large  $|a|$ , the impurity-bath interactions lead to  $a$ -dependent loss of both states on  $t_n$  timescale, which is fast compared to our measurement time and makes a direct measurement of the  $|\downarrow\rangle$  population challenging. Instead, at the end of each experimental sequence we quench  $B \rightarrow B_{\text{res}}$  and wait for all impurities to be lost, so their concentration is faithfully reflected in the fractional loss of the total atom population,  $\Delta N/N$ .

### Injection spectroscopy

In order for the measured injection spectrum,  $I(\omega) \propto \Delta N(\omega)/N$ , to reflect the energy spectrum of the impurity-bath system, we use long pulses  $t_{\text{rf}} \geq 200\mu\text{s} \gg t_n$  and limit the injection fractions to a few percent, to minimize Fourier broadening and stay in the linear response regime.

Figure 1C shows characteristic injection spectra in the strongly interacting regime, plotted as a function of the detuning  $\delta = \omega_0 - \omega$ , where  $\omega_0/(2\pi)$  (of about 0.1 GHz) is the bare transition frequency. For  $1/(k_n a) = -0.56$  (left), we observe a single asymmetric spectral feature peaked at negative  $\delta$ , corresponding to the attractive polaron. For  $1/(k_n a) = 1.00$  (right), we resolve two spectral features: the repulsive polaron peaked at  $\delta > 0$  and the negative-energy molecular state.

In Fig. 1D we show an overview of  $I(\delta)$  for a broad range of  $1/(k_n a)$ , with  $n \approx 12\mu\text{m}^{-3}$ , across the Feshbach resonance at  $B_{\text{res}} = 526.2\text{G}$ ; here  $t_{\text{rf}} = 200\mu\text{s}$  and the rf Rabi frequency

is  $\Omega/(2\pi) \approx 0.6\text{kHz}$ . The black solid line shows the energy of the attractive polaron calculated using a minimal variational model [55], which includes single-phonon excitations of the BEC [33, 48]. Within this theory, the attractive polaron is the ground state, and its energy approaches the dimer energy  $E_d$  (dashed line) at large positive  $1/(k_n a)$ . The repulsive polaron is metastable and vanishes near the resonance; in the region where the repulsive polaron is well-defined, it approximately has the mean-field energy  $2\pi\hbar^2 n a / m_r$  (purple line).

### Real-time dynamics

To probe the real-time impurity dynamics, we use Ramsey-type interferometry [14, 25] outlined in Fig. 2A, which gives the complex coherence function  $C(t) = |C(t)| \exp[i\phi_c(t)]$ , formally related to  $I(\delta)$  by a Fourier transform [56]. Here the first rf pulse (of duration  $t_p \approx 15\mu\text{s}$ ) creates a small coherent admixture of impurities, and the second one, with a variable phase  $\phi$ , probes their evolution; the contrast and phase of the periodic variation of  $\Delta N/N$  with  $\phi$  (see Fig. 2B) give  $|C(t)|$  and  $\phi_c(t)$ , defined so that  $C(0) = 1$ . To resolve ultrafast dynamics (on timescale  $t_n$ ) and avoid effects of finite  $t_p$ , we perform the rf pulses at weak interactions ( $a = \pm 440a_0$ ) and in-between set  $a$  (in  $\sim 2\mu\text{s} \ll t_n$ ) for the evolution time  $t$  using magnetic-field quenches [57], without crossing  $B_{\text{res}}$ .

In Fig. 2C we show  $C(t)$  for various  $1/(k_n a)$  at fixed  $n = 12(1)\mu\text{m}^{-3}$ , for  $B_{\text{res}} = 526.2\text{G}$ . Generally, at long times, both the phase winding and the contrast decay are faster for stronger interactions, but for  $a > 0$  the dynamics are more complex due to beating between the repulsive-polaron and molecular branches [14, 28]; see [54] for more details, including early-time dynamics. In Fig. 2D we show, for three characteristic  $1/(k_n a)$ , that we obtain essentially the same results from interferometry and spectroscopy, but interferometry is intrinsically free of Fourier broadening.

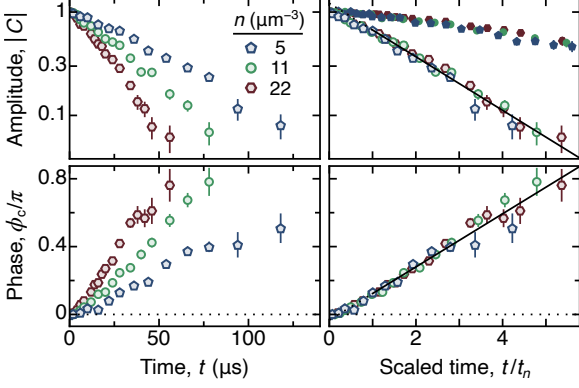


FIG. 3. Universal dynamics at unitarity. Evolution of the coherence-function amplitude  $|C|$  (top) and phase  $\phi_c$  (bottom) for three different bath densities  $n$ . The left panels show the evolution with respect to the real time  $t$ ; for larger  $n$  the dynamics are faster. In the right panels, the same data collapse onto universal curves when plotted versus the scaled time  $t/t_n$ . The solid symbols show an estimate of the decay of  $|C|$  due to atom loss [54]. The solid lines show an exponential-decay fit of  $|C|$  (top) and linear fit of  $\phi_c$  (bottom), for  $t > t_n$ . The error bars show fitting errors.

#### Universal dynamics at unitarity

We now turn to a detailed study of the impurity dynamics at unitarity, where  $a$  diverges and drops out of the problem. In Fig. 3, we show  $C(t)$  for  $B_{\text{res}} = 526.2\text{G}$  and three different  $n$ . The dynamics are naturally faster for larger  $n$  (left), but when plotting versus  $t/t_n$ , both  $|C|$  and  $\phi_c$  data collapse onto universal curves (right). This ‘Fermi-like’ scaling with  $t_n \propto n^{2/3}$ , which implies that the physics is universal and scale-invariant (solely set by  $n$ , which defines the absolute time and energy scales), is a hallmark result for unitary single-component Bose gases [57–60]. Here we observe it for the first time for an impurity interacting with a BEC.

The particle loss during the evolution time  $t$  is not negligible, but this alone explains only a small part of the observed decoherence (see solid symbols in Fig. 3 and [54]). For  $t > t_n$ ,  $|C|$  is consistent with an exponential decay (with inverse lifetime  $0.60(8)/t_n$ ), and  $\phi_c$  is essentially linear (with slope  $0.49(4)/t_n$ ). While the latter is often considered a signature of well-defined quasiparticles, the decoherence is as

fast as the phase winding, which brings into question the validity of the quasiparticle picture. At  $t < t_n$ , the fractional decoherence and loss rates are lower, hinting at a gradual buildup of correlations in the system.

#### Universality of the Bose polaron spectrum

In Fig. 4 we extend our study to a broad range of  $n$  and  $a$ , and to the Feshbach resonance at  $B_{\text{res}} = 445.4\text{G}$ , to also vary  $a_b$ . Here we use the more economical spectroscopic measurements, adjusting  $t_{\text{rf}}$  and  $\Omega$  to minimize Fourier broadening. We characterize the spectra using their mode,  $E_p/\hbar$ , and half width at half maximum,  $\Gamma$  [62]. For  $a > 0$ , in the region with two resolvable spectral branches, we extract  $E_p$  and  $\Gamma$  for each separately [54].

As shown in Fig. 4A, plotting  $E_p/E_n$  versus  $1/(k_n a)$  collapses almost all our data. Such universal behavior is expected if the physics is predominantly set by  $n$  and  $a$ , with other scales (including  $a_b$ ) entering only weakly. Our data hint at a small difference between the two  $a_b$  only for  $1/(k_n a) \approx -1.5$ . For the attractive polaron,  $E_p$  is consistent with the single-phonon ansatz (black line) for  $1/(k_n a) \lesssim -2$ , but for stronger interactions it deviates and tends to a constant near unitarity. For the repulsive polaron,  $E_p$  is close to the mean-field prediction (purple line), while for the molecular branch it is close to  $E_d$  (dashed line).

Figure 4B shows that the dimensionless  $\hbar\Gamma/E_n$  is also predominantly set by  $1/(k_n a)$ . For the two polaron branches, it increases near the resonance, while for the molecular branch it is always large and constant, meaning that  $\Gamma$  is independent of  $a$ . In Fig. 4C, we show that on approaching  $1/(k_n a) = 0$ , for the attractive polaron  $\hbar\Gamma$  rises above  $|E_p|$ , again suggesting a breakdown of the quasiparticle picture, either due to a short lifetime or due to a transfer of spectral weight to a continuum of higher-lying states (see also [24]). For the molecular branch,  $\hbar\Gamma/|E_p|$  similarly increases above unity. The repulsive polaron overlaps with the molecular state and vanishes for  $1/(k_n a) \lesssim 0.5$ , but at all  $1/(k_n a)$  where we can resolve it,  $\hbar\Gamma/|E_p|$  remains below unity. Away from resonance,  $\hbar\Gamma/|E_p|$  is approximately constant for both polaron branches, which can be partially explained by finite-size effects also seen in mean-field simulations [54].

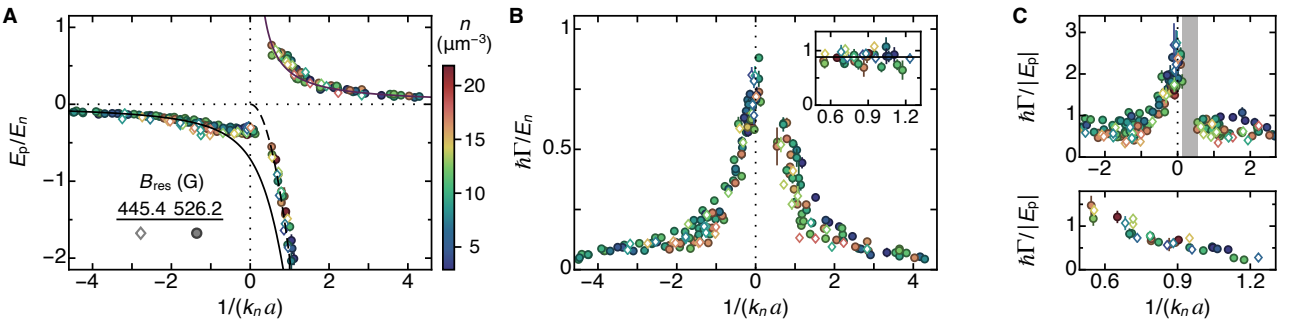


FIG. 4. Universal features of the Bose polaron spectrum. (A,B) Spectrum mode  $E_p$  (A), and half-width at half-maximum  $\hbar\Gamma$  [62] (B), for various densities  $n$  (color bar) and two different Feshbach resonances (legend). When normalized by  $E_n$  and plotted versus the dimensionless interaction parameter  $1/(k_n a)$ , all data essentially collapse onto universal curves. In A, the solid and dashed lines are the same as in Fig. 1D. In B, the main panel shows data for the two polaron branches, and the inset for the molecular one (solid line:  $\hbar\Gamma/E_n = 0.88$ ). (C) Breakdown of the quasiparticle picture. Near resonance,  $\hbar\Gamma$  exceeds  $|E_p|$  for both the attractive polaron (top) and the molecular branch (bottom). The repulsive polaron overlaps with the molecular state and vanishes in the shaded region (top). The error bars reflect fitting errors.

### The molecular branch

Finally, we further investigate the molecular branch. In Fig. 5A, we show spectra for increasing  $n$  at fixed  $E_d/(2\pi\hbar) = -13$  kHz ( $a = 2700a_0$ ), for  $B_{\text{res}} = 526.2$  G [63]. This explicitly shows how the spectrum broadens with  $n$ , while its peak stays roughly at  $E_d/\hbar$  (see also Figs. 4A,B). As shown in Fig. 5B, when normalized by the height of the molecular feature and plotted versus  $(\hbar\delta - E_d)/E_n$ , the molecular spectra collapse onto a universal curve. The asymmetric lineshape (shaded area, see [54]), with a significant tail towards  $\hbar\delta < E_d$ , suggests the existence of many-body state(s) with attractive-polaron character (with energy approximately  $E_n$  below  $E_d$ ). This notion is also supported by the fact that, across the resonance, the lower edge of the molecular branch continuously connects to the attractive polaron (see Fig. 1D).

To corroborate these results, we introduce ‘differential interferometry’ outlined in Fig. 5C, which allows us to isolate the molecular-branch spectrum in the regime where it overlaps with the repulsive-polaron one. We perform two interferometry measurements at the same  $1/(k_n a) \approx 0.6$ , but with the rf pulses performed at either weak attractive or weak repulsive interactions ( $a = \pm 440a_0$ ), and the magnetic field quenches performed in opposite directions. As shown in Fig. 5C, the two protocols result in different relative weights of the two branches: when quenching from  $a < 0$ , across  $B_{\text{res}}$ , the molecular weight is significantly enhanced compared to a quench from  $a > 0$  [64]. Here we normalize the spectra by the height of the repulsive polaron, so that their difference reveals the (unnormalized) molecular-branch contribution (see Fig. 5D), which confirms the key features of the spectrum shown in Fig. 5B.

### Conclusion and outlook

We performed a comprehensive study of the dynamics and spectral features of impurities strongly interacting with a homogeneous BEC. We reveal remarkably universal behavior set by the dimensionless interaction parameter  $1/(k_n a)$  and energy  $E_n$ , defined by the bath density. The molecular branch associated with the Feshbach dimer shows a many-body character, and our measurements near unitarity indicate a breakdown of the quasiparticle picture, but even these effects respect the universal  $E_n$  scaling. Our homogeneous system and the ability to resolve the repulsive polaron and the molecular branch will be crucial for future studies, including the effects of non-zero temperature [66–68], mediated interactions between polarons [69, 70], and their thermodynamic and transport properties.

We thank Martin Gazo, Georg Bruun, Martin Zwierlein, Richard Schmidt, Arthur Christianen, Meera Parish, Jesper Levinsen, Fabian Grusdt, and Eugene Demler for discussions. This work was supported by EPSRC [Grant No. EP/P009565/1], ERC [UniFlat], and STFC [Grant No. ST/T006056/1]. Z.H. acknowledges support from the Royal Society Wolfson Fellowship. C. E. acknowledges support from Jesus College (Cambridge).

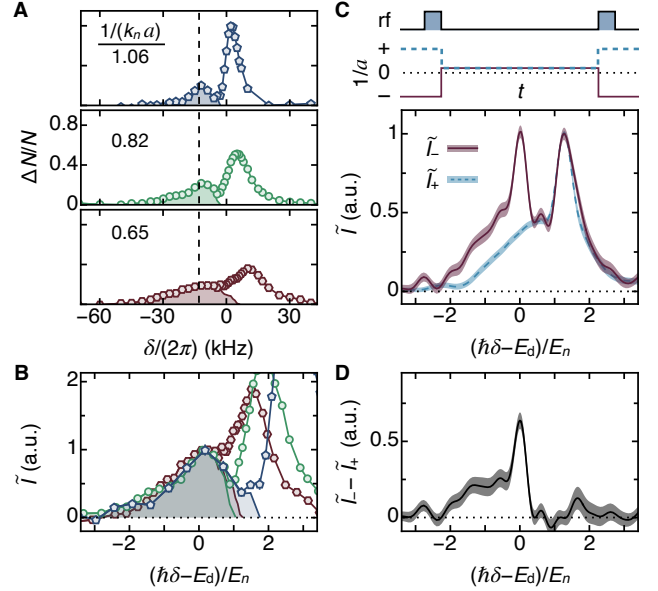


FIG. 5. The molecular branch. (A) Injection spectra for varying density  $n$  at  $a = 2700a_0$ ,  $E_d/(2\pi\hbar) = -13$  kHz (dashed line). The shading shows the molecular contribution, obtained by subtracting a fit to the repulsive polaron (see [54]). (B) When normalized by its peak and plotted versus  $(\hbar\delta - E_d)/E_n$ , the molecular part of  $I(\delta)$  collapses onto a universal asymmetric curve. (C) Differential interferometry. Changing the direction of the interaction quench (top) changes the relative weights of the polaron and molecular branches. The resulting spectra  $\tilde{I}_-$  and  $\tilde{I}_+$  (for quenches from negative and positive  $a$ , respectively), normalized by the height of the repulsive polaron peak; here  $1/(k_n a) \approx 0.6$  and  $n \approx 13 \mu \text{m}^{-3}$ . (D) The difference  $\tilde{I}_- - \tilde{I}_+$  reveals the molecular spectrum, with the same peak and asymmetry as in B. The error bars and line thicknesses reflect measurement uncertainties.

<sup>†</sup> Present address: JILA, NIST, and Department of Physics, University of Colorado, Boulder, Colorado 80309, USA

\* ce330@cam.ac.uk

- [1] G. Baym and C. Pethick, *Landau Fermi-Liquid Theory* (Wiley-VCH, 2004).
- [2] L. Pitaevskii and S. Stringari, *Bose-Einstein condensation and superfluidity* (Oxford University Press, Oxford, 2016).
- [3] L. D. Landau, Electron Motion in Crystal Lattices, *Phys. Z. Sowjet.* **3**, 664 (1933).
- [4] S. I. Pekar, Autolocalization of the Electron in an Inertially Polarizable Dielectric Medium, *Zh. Eksp. Teor. Fiz.* **16**, 335 (1946).
- [5] A. S. Alexandrov, ed., *Polarons in Advanced Materials* (Springer, 2008).
- [6] C. Franchini, M. Reticcioli, M. Setvin, and U. Diebold, Polarons in materials, *Nat. Rev. Mater.* **6**, 560 (2021).
- [7] M. Tomza, K. Jachymski, R. Gerritsma, A. Negretti, T. Calarco, Z. Idziaszek, and P. S. Julienne, Cold hybrid ion-atom systems, *Rev. Mod. Phys.* **91**, 035001 (2019).
- [8] A. Schirotzek, C.-H. Wu, A. Sommer, and M. W. Zwierlein, Observation of Fermi Polarons in a Tunable Fermi Liquid of Ultracold Atoms, *Phys. Rev. Lett.* **102**, 230402 (2009).
- [9] S. Nascimbène, N. Navon, K. J. Jiang, L. Tarruell, M. Teichmann, J. McKeever, F. Chevy, and C. Salomon, Collective Oscillations of an Imbalanced Fermi Gas: Axial Compression Modes and Polaron Effective Mass, *Phys. Rev. Lett.* **103**, 170402 (2009).
- [10] C. Kohstall, M. Zaccanti, M. Jag, A. Trenkwalder, P. Massig

nan, G. M. Bruun, F. Schreck, and R. Grimm, Metastability and coherence of repulsive polarons in a strongly interacting Fermi mixture, *Nature* **485**, 615 (2012).

[11] M. Koschorreck, D. Pertot, E. Vogt, B. Fröhlich, M. Feld, and M. Köhl, Attractive and repulsive Fermi polarons in two dimensions, *Nature* **485**, 619 (2012).

[12] Y. Zhang, W. Ong, I. Arakelyan, and J. E. Thomas, Polaron-to-Polaron Transitions in the Radio-Frequency Spectrum of a Quasi-Two-Dimensional Fermi Gas, *Phys. Rev. Lett.* **108**, 235302 (2012).

[13] A. N. Wenz, G. Zürn, S. Murmann, I. Brouzos, T. Lompe, and S. Jochim, From Few to Many: Observing the Formation of a Fermi Sea One Atom at a Time, *Science* **342**, 457 (2013).

[14] M. Cetina, M. Jag, R. S. Lous, I. Fritzsche, J. T. M. Walraven, R. Grimm, J. Levinsen, M. M. Parish, R. Schmidt, M. Knap, and E. Demler, Ultrafast many-body interferometry of impurities coupled to a Fermi sea, *Science* **354**, 96 (2016).

[15] F. Scazza, G. Valtolina, P. Massignan, A. Recati, A. Amico, A. Burchianti, C. Fort, M. Inguscio, M. Zaccanti, and G. Roati, Repulsive Fermi Polarons in a Resonant Mixture of Ultracold  $^6\text{Li}$  Atoms, *Phys. Rev. Lett.* **118**, 083602 (2017).

[16] N. Darkwah Oppong, L. Riegger, O. Bettermann, M. Höfer, J. Levinsen, M. M. Parish, I. Bloch, and S. Fölling, Observation of Coherent Multiorbital Polarons in a Two-Dimensional Fermi Gas, *Phys. Rev. Lett.* **122**, 193604 (2019).

[17] Z. Yan, P. B. Patel, B. Mukherjee, R. J. Fletcher, J. Struck, and M. W. Zwierlein, Boiling a Unitary Fermi Liquid, *Phys. Rev. Lett.* **122**, 093401 (2019).

[18] G. Ness, C. Shkedrov, Y. Florshaim, O. K. Diessel, J. von Milczewski, R. Schmidt, and Y. Sagi, Observation of a Smooth Polaron-Molecule Transition in a Degenerate Fermi Gas, *Phys. Rev. X* **10**, 041019 (2020).

[19] F. J. Vivanco, A. Schuckert, S. Huang, G. L. Schumacher, G. G. T. Assumpção, Y. Ji, J. Chen, M. Knap, and N. Navon, The strongly driven Fermi polaron, *arXiv:2308.05746* (2023).

[20] C. Baroni, B. Huang, I. Fritzsche, E. Dobler, G. Anich, E. Kirillov, R. Grimm, M. A. Bastarrachea-Magnani, P. Massignan, and G. M. Bruun, Mediated interactions between Fermi polarons and the role of impurity quantum statistics, *Nat. Phys.* **20**, 68 (2024).

[21] N. B. Jørgensen, L. Wacker, K. T. Skalmstang, M. M. Parish, J. Levinsen, R. S. Christensen, G. M. Bruun, and J. J. Arlt, Observation of Attractive and Repulsive Polarons in a Bose-Einstein Condensate, *Phys. Rev. Lett.* **117**, 055302 (2016).

[22] M.-G. Hu, M. J. Van de Graaff, D. Kedar, J. P. Corson, E. A. Cornell, and D. S. Jin, Bose Polarons in the Strongly Interacting Regime, *Phys. Rev. Lett.* **117**, 055301 (2016).

[23] T. Rentrop, A. Trautmann, F. A. Olivares, F. Jendrzejewski, A. Komnik, and M. K. Oberthaler, Observation of the Phononic Lamb Shift with a Synthetic Vacuum, *Phys. Rev. X* **6**, 041041 (2016).

[24] Z. Z. Yan, Y. Ni, C. Robens, and M. W. Zwierlein, Bose polarons near quantum criticality, *Science* **368**, 190 (2020).

[25] M. G. Skou, T. G. Skov, N. B. Jørgensen, K. K. Nielsen, A. Camacho-Guardian, T. Pohl, G. M. Bruun, and J. J. Arlt, Non-equilibrium quantum dynamics and formation of the Bose polaron, *Nat. Phys.* **17**, 731 (2021).

[26] M. G. Skou, K. K. Nielsen, T. G. Skov, A. M. Morgen, N. B. Jørgensen, A. Camacho-Guardian, T. Pohl, G. M. Bruun, and J. J. Arlt, Life and death of the Bose polaron, *Phys. Rev. Res.* **4**, 043093 (2022).

[27] H. Cayla, P. Massignan, T. Giamarchi, A. Aspect, C. I. Westbrook, and D. Clément, Observation of  $1/k^4$ -Tails after Expansion of Bose-Einstein Condensates with Impurities, *Phys. Rev. Lett.* **130**, 153401 (2023).

[28] A. M. Morgen, S. S. Balling, K. K. Nielsen, T. Pohl, G. M. Bruun, and J. J. Arlt, Quantum beat spectroscopy of repulsive Bose polarons, *arXiv:2310.18183* (2023).

[29] See also recent related studies in semiconductors [30, 31].

[30] L. B. Tan, O. K. Diessel, A. Popert, R. Schmidt, A. Imamoglu, and M. Krömer, Bose polaron interactions in a cavity-coupled monolayer semiconductor, *Phys. Rev. X* **13**, 031036 (2023).

[31] D. Huang, K. Sampson, Y. Ni, Z. Liu, D. Liang, K. Watanabe, T. Taniguchi, H. Li, E. Martin, J. Levinsen, M. M. Parish, E. Tutuc, D. K. Efimkin, and X. Li, Quantum Dynamics of Attractive and Repulsive Polarons in a Doped  $\text{MoSe}_2$  Monolayer, *Phys. Rev. X* **13**, 011029 (2023).

[32] C. Chin, R. Grimm, P. Julienne, and E. Tiesinga, Feshbach resonances in ultracold gases, *Rev. Mod. Phys.* **82**, 1225 (2010).

[33] S. P. Rath and R. Schmidt, Field-theoretical study of the Bose polaron, *Phys. Rev. A* **88**, 053632 (2013).

[34] A. Christianen, J. I. Cirac, and R. Schmidt, Phase diagram for strong-coupling Bose polarons, *arXiv:2306.09075* (2023).

[35] P. Massignan, M. Zaccanti, and G. M. Bruun, Polarons, dressed molecules and itinerant ferromagnetism in ultracold Fermi gases, *Rep. Prog. Phys.* **77**, 034401 (2014).

[36] M. M. Parish and J. Levinsen, Fermi polarons and beyond, *arXiv:2306.01215* (2023).

[37] Y. E. Shchadilova, R. Schmidt, F. Grusdt, and E. Demler, Quantum Dynamics of Ultracold Bose Polarons, *Phys. Rev. Lett.* **117**, 113002 (2016).

[38] F. Grusdt, R. Schmidt, Y. E. Shchadilova, and E. Demler, Strong-coupling Bose polarons in a Bose-Einstein condensate, *Phys. Rev. A* **96**, 013607 (2017).

[39] A. Christianen, J. I. Cirac, and R. Schmidt, Bose polaron and the Efimov effect: A Gaussian-state approach, *Phys. Rev. A* **105**, 053302 (2022).

[40] J. Levinsen, M. M. Parish, and G. M. Bruun, Impurity in a Bose-Einstein Condensate and the Efimov Effect, *Phys. Rev. Lett.* **115**, 125302 (2015).

[41] L. A. Peña Ardila and S. Giorgini, Impurity in a Bose-Einstein condensate: Study of the attractive and repulsive branch using quantum Monte Carlo methods, *Phys. Rev. A* **92**, 033612 (2015).

[42] M. Sun, H. Zhai, and X. Cui, Visualizing the Efimov Correlation in Bose Polarons, *Phys. Rev. Lett.* **119**, 013401 (2017).

[43] S. M. Yoshida, S. Endo, J. Levinsen, and M. M. Parish, Universality of an Impurity in a Bose-Einstein Condensate, *Phys. Rev. X* **8**, 011024 (2018).

[44] M. Drescher, M. Salmhofer, and T. Enss, Theory of a resonantly interacting impurity in a Bose-Einstein condensate, *Phys. Rev. Res.* **2**, 032011 (2020).

[45] P. Massignan, N. Yegovtsev, and V. Gurarie, Universal Aspects of a Strongly Interacting Impurity in a Dilute Bose Condensate, *Phys. Rev. Lett.* **126**, 123403 (2021).

[46] R. Schmidt and T. Enss, Self-stabilized Bose polarons, *SciPost Phys.* **13**, 054 (2022).

[47] N. Mostaan, N. Goldman, and F. Grusdt, A unified theory of strong coupling Bose polarons: From repulsive polarons to non-Gaussian many-body bound states, *arXiv:2305.00835* (2023).

[48] W. Li and S. Das Sarma, Variational study of polarons in Bose-Einstein condensates, *Phys. Rev. A* **90**, 013618 (2014).

[49] N. Navon, R. P. Smith, and Z. Hadzibabic, Quantum gases in optical boxes, *Nat. Phys.* **17**, 1334 (2021).

[50] A. L. Gaunt, T. F. Schmidutz, I. Gotlibovych, R. P. Smith, and Z. Hadzibabic, Bose-Einstein Condensation of Atoms in a Uniform Potential, *Phys. Rev. Lett.* **110**, 200406 (2013).

[51] C. Eigen, A. L. Gaunt, A. Suleymanzade, N. Navon, Z. Hadzibabic, and R. P. Smith, Observation of Weak Collapse in a Bose-Einstein Condensate, *Phys. Rev. X* **6**, 041058 (2016).

[52] J. Etrych, G. Martirosyan, A. Cao, J. A. P. Glidden, L. H. Dogra, J. M. Hutson, Z. Hadzibabic, and C. Eigen, Pinpointing Feshbach resonances and testing Efimov universalities in  $^{39}\text{K}$ , *Phys. Rev. Res.* **5**, 013174 (2023).

[53] We have refined the value of  $B_{\text{res}}$  for the  $|1,0\rangle - |1,-1\rangle$  Feshbach resonance to 526.16(3) G, compared to the previously reported 526.21(5) G [52], by extending the thermal-gas  $E_d$  mea-

surements.

[54] Supplementary Material.

[55] F. Chevy, Universal phase diagram of a strongly interacting Fermi gas with unbalanced spin populations, *Phys. Rev. A* **74**, 063628 (2006).

[56] A. Shashi, F. Grusdt, D. A. Abanin, and E. Demler, Radio-frequency spectroscopy of polarons in ultracold Bose gases, *Phys. Rev. A* **89**, 053617 (2014).

[57] C. Eigen, J. A. P. Glidden, R. Lopes, N. Navon, Z. Hadzibabic, and R. P. Smith, Universal Scaling Laws in the Dynamics of a Homogeneous Unitary Bose Gas, *Phys. Rev. Lett.* **119**, 250404 (2017).

[58] T.-L. Ho, Universal Thermodynamics of Degenerate Quantum Gases in the Unitarity Limit, *Phys. Rev. Lett.* **92**, 090402 (2004).

[59] C. E. Klauss, X. Xie, C. Lopez-Abadia, J. P. D’Incao, Z. Hadzibabic, D. S. Jin, and E. A. Cornell, Observation of Efimov Molecules Created from a Resonantly Interacting Bose Gas, *Phys. Rev. Lett.* **119**, 143401 (2017).

[60] See also [61], for related results on particle loss in a Bose–Fermi mixture.

[61] S. Laurent, M. Pierce, M. Delehaye, T. Yefsah, F. Chevy, and C. Salomon, Connecting Few-Body Inelastic Decay to Quantum Correlations in a Many-Body System: A Weakly Coupled Impurity in a Resonant Fermi Gas, *Phys. Rev. Lett.* **118**, 103403 (2017).

[62] We correct  $\Gamma$  for residual finite- $t_{\text{rf}}$  broadening, see [54] for details.

[63] Note that here we resort to stronger rf pulses to improve the signal of the molecular branch, potentially compromising the linear response regime for the repulsive polaron.

[64] Effects of the initial interaction strength on spectral weight (without crossing the resonance) were observed in [14] for the Fermi polaron. More generally, the possibility of creating a coherent superposition of atoms and molecules using field quenches was first shown in [65].

[65] E. A. Donley, N. R. Claussen, S. T. Thompson, and C. E. Wieman, Atom-molecule coherence in a Bose–Einstein condensate, *Nature* **417**, 529 (2002).

[66] N.-E. Guenther, P. Massignan, M. Lewenstein, and G. M. Bruun, Bose polarons at finite temperature and strong coupling, *Phys. Rev. Lett.* **120**, 050405 (2018).

[67] B. Field, J. Levinsen, and M. M. Parish, Fate of the Bose polaron at finite temperature, *Phys. Rev. A* **101**, 013623 (2020).

[68] G. Pascual and J. Boronat, Quasiparticle Nature of the Bose Polaron at Finite Temperature, *Phys. Rev. Lett.* **127**, 205301 (2021).

[69] A. Camacho-Guardian and G. M. Bruun, Landau Effective Interaction between Quasiparticles in a Bose-Einstein Condensate, *Phys. Rev. X* **8**, 031042 (2018).

[70] A. Camacho-Guardian, L. A. Peña Ardila, T. Pohl, and G. M. Bruun, Bipolarons in a Bose-Einstein Condensate, *Phys. Rev. Lett.* **121**, 013401 (2018).

[71] E. A. Donley, N. R. Claussen, S. L. Cornish, J. L. Roberts, E. A. Cornell, and C. E. Wieman, Dynamics of collapsing and exploding Bose–Einstein condensates, *Nature* **412**, 295 (2001).

[72] G. Martirosyan, C. J. Ho, J. Etrych, Y. Zhang, A. Cao, Z. Hadzibabic, and C. Eigen, Observation of Subdiffusive Dynamic Scaling in a Driven and Disordered Bose Gas, *arXiv:2304.06697* (2023).

## SUPPLEMENTARY MATERIAL

## Preparation and measurement

Our optical box trap is cylindrical (radius  $R$ , length  $L$ ), and to increase the range of densities we can explore, we use either  $R \approx 14 \mu\text{m}$  and  $L \approx 45 \mu\text{m}$  or  $R \approx 10 \mu\text{m}$  and  $L \approx 30 \mu\text{m}$ , with a trap depth  $U_D \approx k_B \times 50 \text{nK}$ . Our experiments always start with a quasi-pure spin-polarized BEC in  $|F, m_F\rangle = |1, 1\rangle$ , and we then transfer the atoms to either  $|1, 0\rangle$  or  $|1, -1\rangle$  (our two bath states) using Landau-Zener rf sweeps.

For preparing the  $|1, 0\rangle$  bath, we transfer the BEC from  $|1, 1\rangle$  to  $|1, 0\rangle$  at  $B = 396 \text{ G}$  [51], where both intrastate scattering lengths,  $a_{1,1}$  and  $a_{0,0}$ , are positive (see Fig. S1). For preparing the  $|1, -1\rangle$  bath, we cannot simply transfer the BEC from  $|1, 0\rangle$  to  $|1, -1\rangle$ , because there is no  $B$  at which both  $a_{0,0}$  and  $a_{-1,-1}$  are positive, and attractive interactions would lead to BEC collapse [51, 71]. To circumvent this, at  $B = 396 \text{ G}$  we temporarily create a highly nonthermal state with destroyed coherence but same particle number and low energy per particle, by shaking the cloud with a periodic force [72]. This allows us to transfer the atoms to  $|1, -1\rangle$  without collapse, then ramp  $B$  to  $\approx 550 \text{ G}$  where  $a_{-1,-1} > 0$ , and recondense the cloud, achieving a final quasi-pure BEC with about 80% of the atoms in the initial  $|1, 1\rangle$  condensate.

We levitate the bath atoms against gravity using a magnetic field gradient. Owing to the small difference in magnetic moments between the bath and impurity states (3% for  $|1, 0\rangle$  and  $|1, 1\rangle$  at  $445.2 \text{ G}$ , and 0.3% for  $|1, -1\rangle$  and  $|1, 0\rangle$  at  $526.2 \text{ G}$ ), impurities are also essentially levitated.

The impurity-impurity interactions are attractive with  $a_i \approx -64(1)a_0$  in both cases, but are not relevant on our experimental timescales due to the small impurity concentration.

At the end of the experimental sequence, we measure the total atom number after time of flight expansion (typically for 60 ms) using absorption imaging at low  $B$ .

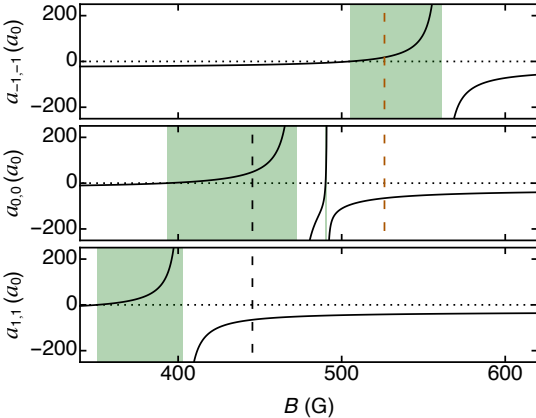


FIG. S1. Intrastate Feshbach resonance landscape for  $^{39}\text{K}$  in the  $F = 1$  manifold [52]; here we denote the different scattering lengths  $a_{m_F, m_F}$ . The dashed lines indicate  $B_{\text{res}}$  of the two interstate Feshbach resonances used to tune impurity-bath interactions. The green shaded areas highlight regions where  $a_{m_F, m_F} > 0$ .

## Extraction of impurity spectra

In the linear response regime, injection spectroscopy reveals the impurity spectral function  $A(\omega)$ . For a square rf pulse of duration  $t_{\text{rf}}$ , the spectrum is approximately:

$$I(\omega) = \frac{t_{\text{rf}}}{2\pi} \int_{-\infty}^{\infty} A(\omega') \text{sinc} \left[ \frac{(\omega - \omega') t_{\text{rf}}}{2} \right]^2 d\omega', \quad (\text{S1})$$

normalized such that  $\int I(\omega) d\omega = 1$ .

For a weak pulse, the fraction of atoms transferred from  $|\uparrow\rangle$  to  $|\downarrow\rangle$  is  $(\Omega^2 t_{\text{rf}} \pi / 2) I(\omega)$ , where  $\Omega$  is the Rabi frequency. In the experiment, we instead measure the total loss fraction (following a quench to  $B_{\text{res}}$ ), which is related to the transfer fraction by a constant of proportionality  $\alpha$ , so that  $\Delta N/N = (\alpha \Omega^2 t_{\text{rf}} \pi / 2) I(\omega)$ . We experimentally estimate  $\alpha \approx 4$  based on loss measurements at unitarity.

In Fig. 1D, we normalize the spectra using  $t_{\text{rf}} = 200 \mu\text{s}$ ,  $\alpha = 4$ , and estimated  $\Omega/(2\pi) = 0.6 \text{ kHz}$  (based on the average area). In Fig. 2D, we normalize all spectra individually based on their numerically estimated area.

The spectral function can be also calculated from the coherence function  $C(t)$ :

$$A(\omega) = \frac{1}{\pi} \text{Re} \left[ \int_0^{\infty} C(t) e^{-i\omega t} dt \right]. \quad (\text{S2})$$

To numerically compute the Fourier transform, we use piecewise linear interpolations of  $|C|$  and  $\phi_c$ . We assess the uncertainty in  $A(\omega)$  by repeating the procedure with points randomly sampled within their experimental errors. For comparison with spectroscopic data (Fig. 2D), we can take into account Fourier broadening using Eq. (S1).

Our experimental  $B$ -field stability is  $\sim 10 \text{ mG}$ , corresponding to  $\pm 0.03 \text{ kHz}$  and  $\pm 0.4 \text{ kHz}$  uncertainty in  $\omega_0/(2\pi)$  near  $B_{\text{res}} = 526 \text{ G}$  and  $445 \text{ G}$ , respectively. We also correct for the small shift in  $\delta$  due to the mean-field energy of the bath atoms,  $\delta_{\text{mf}} = 4\pi\hbar n a_b/m$ , where  $m$  is the atom mass.

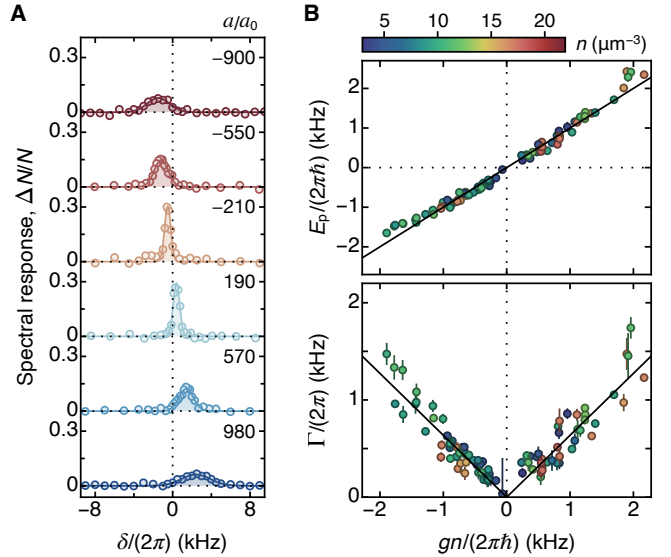


FIG. S2. Injection spectroscopy in the weakly interacting regime. (A) Injection spectra for  $n = 12(1) \mu\text{m}^{-3}$  and varying  $a$ , for  $B_{\text{res}} = 526.2 \text{ G}$ ; here  $t_{\text{rf}} = 1600 \mu\text{s}$ . The solid lines show Gaussian fits used to extract the mode  $E_p$  and half-width-half-maximum  $\Gamma$  [62]. (B) Plot of  $E_p$  (top) and  $\Gamma$  (bottom) versus  $gn$  for a range of  $n$  and  $a$ . The solid lines show  $E_p = gn$  (top) and  $\Gamma = 0.64|g|\hbar$  (bottom).

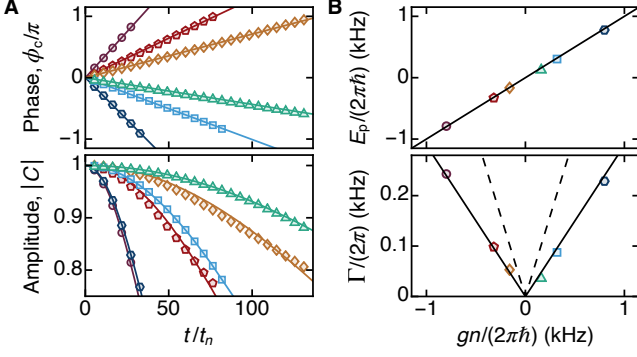


FIG. S3. Mean-field simulations of Ramsey interferometry. (A) Phase and amplitude of  $C(t)$  for varying  $a$  (indicated by the symbols, see B). The solid lines show fits to  $\phi_c$  and  $|C|$ . (B) Extracted  $E_p$  (top) and rate of decoherence  $\Gamma$  (bottom) versus  $gn$  (see text). The solid lines show  $E_p = gn$  (top) and  $\Gamma = 0.3|g|n$  (bottom). The dashed line shows  $\Gamma = 0.64|g|n$  from experiments.

#### Injection spectroscopy at low $a$ and density calibration

In Fig. S2 we show injection spectra for  $1/(k_n|a|) > 2$ . As shown in Fig. S2A, we observe essentially symmetric spectra and we extract  $E_p$  and  $\Gamma$  using Gaussian fits. For sufficiently weak interactions, we observe a linear dependence of  $E_p$  on  $a$  (see Fig. S2B, top). We calibrate the effective volume of our two boxes so that a linear fit to the data with shifts  $< 1$  kHz recovers the mean-field result  $E_p = gn$ , with  $g = 2\pi\hbar^2 a/m_r$ ; note that we also independently correct for small changes in the effective box volume based on the chemical potential of the bath.

The half-width  $\Gamma$  [62] is also roughly proportional to  $gn$  (see Fig. S2B, bottom). This unexpected dependence is heuristically captured by  $\Gamma = 0.64|g|n$  (solid line).

#### Mean-field simulations

We simulate our system on the mean-field level using the two-component Gross–Pitaevskii equation

$$\begin{aligned} i\hbar \frac{\partial \psi_\uparrow}{\partial t} &= -\frac{\hbar^2}{2m} \nabla^2 \psi_\uparrow + g_{\uparrow\uparrow} |\psi_\uparrow|^2 \psi_\uparrow + g_{\uparrow\downarrow} |\psi_\downarrow|^2 \psi_\uparrow \\ i\hbar \frac{\partial \psi_\downarrow}{\partial t} &= -\frac{\hbar^2}{2m} \nabla^2 \psi_\downarrow + g_{\downarrow\downarrow} |\psi_\downarrow|^2 \psi_\downarrow + g_{\downarrow\uparrow} |\psi_\uparrow|^2 \psi_\downarrow, \end{aligned} \quad (\text{S3})$$

with  $g_{\uparrow\uparrow} = 4\pi\hbar^2 a_b/m$ ,  $g_{\downarrow\downarrow} = 4\pi\hbar^2 a_i/m$  and  $g_{\uparrow\downarrow} = g = 2\pi\hbar^2 a/m_r$ . We use a pseudo-spectral method with fourth-order Runge–Kutta time evolution to solve Eqs. (S3), performed on a  $64 \times 64 \times 128$  grid with dimensions  $40 \times 40 \times 80 \mu\text{m}^3$  and a  $4 \mu\text{s}$  time-step. Our simulations start from the ground-state wavefunction of  $N$  particles in  $|\uparrow\rangle$  state,  $\psi_0$ , obtained through imaginary-time evolution. To obtain  $C(t)$ , we initiate the real-time dynamics with  $\psi_1 = \sqrt{1-f}\psi_0$  and  $\psi_\downarrow = \sqrt{f}\psi_0$ , where  $f$  is the impurity fraction, wait for an evolution time  $t$ , and calculate  $C(t) = \langle \psi_\downarrow(t) | \psi_\downarrow(t) \rangle / \langle \psi_\downarrow(0) | \psi_\downarrow(0) \rangle$ . We note that for all experimental combinations of  $a$ ,  $a_b$ ,  $a_i$ , the two-component mixture is mean-field unstable. At long times, we observe signatures of wavefunction collapse and associated numerical instability, but initially, the dynamics are well-defined.

In Fig. S3A, we show the evolution of  $C(t)$  for varying  $a$ , with  $a_b = 18a_0$ ,  $a_i = -64a_0$ ,  $N = 2.7 \times 10^5$ ,  $f = 0.05$ , and a perfect box potential with  $R = 15 \mu\text{m}$ ,  $L = 50 \mu\text{m}$ , and depth of  $50 \text{nK}$ . We estimate  $E_p$  and  $\Gamma$  using linear and Gaussian fits to  $\phi_c$  and  $|C|$ , respectively. The extracted  $E_p$  is consistent with  $E_p = gn$ , where  $n = \int |\psi_\uparrow|^4 d^3\mathbf{r}/N$  is the average bath density. We find  $\Gamma \approx 0.3|g|n$ , which captures the experimentally observed  $\Gamma \propto |g|n$  scaling (see Fig. S2B), but not its absolute value. We attribute this decoherence to dynamics arising from the sudden quench of an effective potential felt by the impurities, given by  $gn(\mathbf{r}) = g|\psi_\uparrow(\mathbf{r})|^2$ , which varies over the healing length  $\xi = 1/\sqrt{8\pi n a_b}$  near box edges (in Fig. S3  $\xi \approx 2 \mu\text{m}$ ).

We have also checked that we obtain essentially the same results with  $a_i = 0$  and  $a_i = +64a_0$ , indicating that for small transfer fractions the impurity–impurity interactions do not play a significant role.

#### Extraction of $E_p$ and $\Gamma$

Here we detail our extraction of the mode  $E_p$  and half-width  $\Gamma$  of  $I(\delta)$ . In Fig. S4, we exemplify this for different characteristic  $1/(k_n a)$  in the strongly interacting regime, where the lineshapes are no longer Gaussian. The polaron features are clearly asymmetric, with a tail to larger  $\delta$ . We heuristically fit the spectra using the combination of a Gaussian (for  $\delta < E_p/\hbar$ ) and a Lorentzian (for  $\delta > E_p/\hbar$ ), faithfully capturing  $E_p$  and  $\Gamma$ .

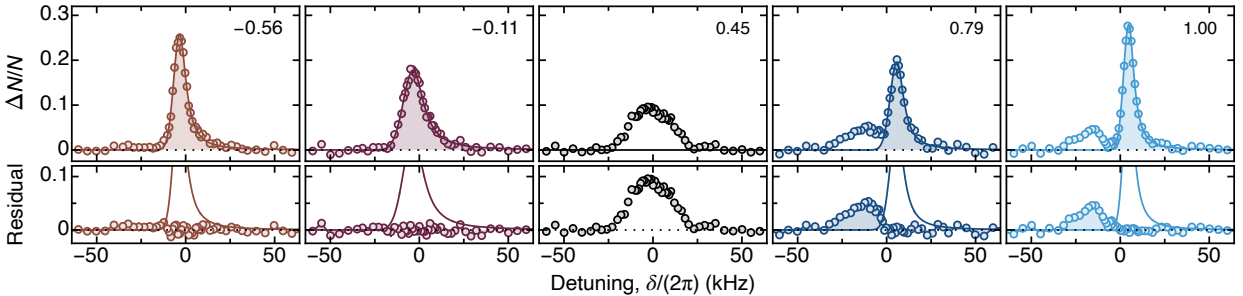


FIG. S4. Extraction of  $E_p$  and  $\Gamma$ . (Top) Examples of  $I(\delta)$  at different  $1/(k_n a)$  (colors) and the polaron spectrum fits (see text). (Bottom) Subtraction of the polaron fit reveals the molecular spectrum for  $1/(k_n a) > 0.5$ . At  $1/(k_n a) = 0.45$ , the two branches cannot be resolved.

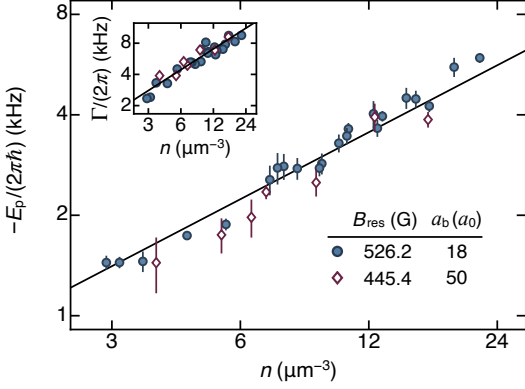


FIG. S5. Scaling laws at unitarity. Extracted mode  $E_p$  (main panel) and width  $\Gamma$  (inset) of  $I(\delta)$  as a function of density  $n$  and for our two  $a_b$  (legend), varying  $k_n a_b$  by a factor of  $\approx 5$ . The solid lines show  $E_p = -0.34E_n$  and  $\hbar\Gamma = 0.68E_n$ .

In the cases where we resolve both the repulsive polaron and the molecular state, we first fit the repulsive polaron spectrum over a constrained range, and then subtract this fit to obtain the molecular contribution to the spectrum. We refrain from extracting  $E_p$  and  $\Gamma$  between  $0.2 \lesssim 1/(k_n a) \lesssim 0.5$  (see example at  $1/(k_n a) = 0.45$  in Fig. S4).

We always correct  $\Gamma$  for Fourier broadening using  $\Gamma = (\Gamma_e^2 - \Gamma_t^2)^{1/2}$ , where  $\Gamma_e$  is the raw extracted width and  $\Gamma_t \approx 2.78/t_{rf}$  is the width of the response function in Eq. (S1).

#### Scaling laws and atom loss at unitarity

Here we explicitly verify the universal  $\propto n^{2/3}$  scaling at unitarity using spectroscopic measurements for both Feshbach resonances, complementing Fig. 3. In Fig. S5 we show the data from Fig. 4 near unitarity ( $-0.2 \lesssim 1/(k_n a) \lesssim 0.2$ ), plotting  $E_p$  versus  $n$  for the two  $a_b$  on log-log scale. We observe no discernible dependence on  $a_b$  (within errors), and a power-law fit gives  $E_p \propto n^\gamma$ , with  $\gamma = 0.7(1)$ . Similarly, we also find that  $\Gamma \propto n^\gamma$ , with  $\gamma = 0.7(1)$  (see inset). These results are consistent with  $\gamma = 2/3$ , expected from the density set  $E_n$  scaling. Assuming  $\gamma = 2/3$  and including systematic uncertainties in  $n$ , we find  $E_p = 0.34(4)E_n$  and  $\Gamma = 0.68(7)E_n$  (solid lines Fig. S5). These results further imply that in our parameter range the spectral function can only depend weakly on  $a_b$  and other lengthscales.

To measure the atom loss at unitarity we perform a short rf pulse at weak interactions and then quench the field to unitarity for a variable hold time (this protocol is equivalent to the Ramsey protocol (Fig. 2A) without the second pulse). We do not resolve impurities and bath atoms separately (our low-field absorption imaging is not state selective), but measure the total fractional atom loss  $\Delta N/N$ . We estimate the decoherence due to this loss (shown as solid symbols in Fig. 3B) using:

$$|C(t)| = \sqrt{\frac{\Delta N_{\max} - \Delta N(t)}{\Delta N_{\max}}}, \quad (\text{S4})$$

where  $\Delta N_{\max}$  is the number of atoms lost at long times (when all impurities have been lost), which assumes that the fractional loss rate is much higher for impurities than bath atoms (satisfied for small impurity fractions).

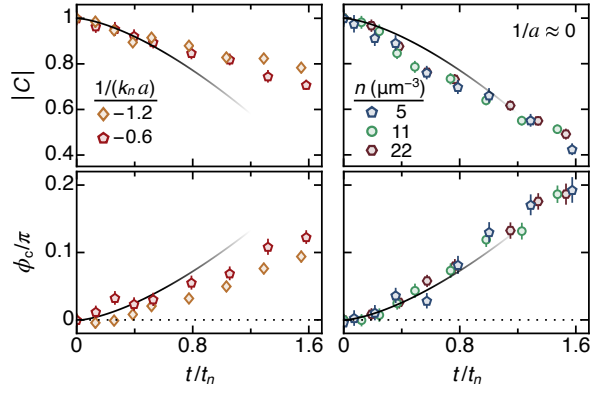


FIG. S6. Early-time  $C(t)$  dynamics for attractive (left) and unitarity (right) interactions (data from Fig. 2C and Fig. 3). The solid lines show the early-time prediction of Ref. [25] [see Eq. (S5)].

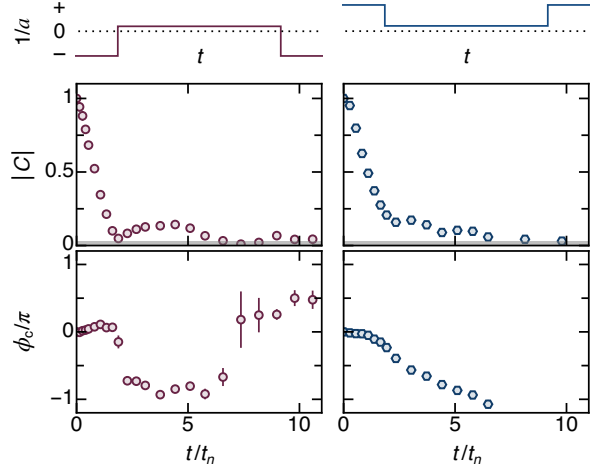


FIG. S7. Dynamics of  $C(t)$  for the two measurements from Fig. 5C, using quenches from either  $a < 0$  (left) or  $a > 0$  (right).

#### Additional details of $C(t)$ evolution

In Fig. S6, we compare the early-time evolution of  $C(t)$  for  $1/(k_n a) \leq 0$  with the two-body universal prediction of Ref. [25], which at short times has the limiting form:

$$|C(t)| = 1 - \frac{16}{9\pi^{3/2}} \left( \frac{t}{t_n} \right)^{3/2} \quad (\text{S5})$$

$$\phi_c(t) = \frac{16}{9\pi^{3/2}} \left( \frac{t}{t_n} \right)^{3/2}.$$

For  $1/(k_n a) = -0.6$  and  $-1.2$ , the initial dynamics agree well with Eqs. (S5), before bending off at longer times, while for  $1/(k_n a) \approx 0$  the dynamics are even faster than the prediction.

In Fig. S7, we show the raw  $C(t)$  data for  $\tilde{I}_\pm$  in Fig. 5C. For the quench from  $a < 0$  we observe clear beating between the two states, with characteristic  $\pi$ -jumps in phase when  $C(t)$  nears zero (see also [14]).

#### Further comparison between spectroscopy and interferometry

In Fig. S8 we compare the  $E_p$  and  $\Gamma$  [62] values of the polaron feature from Fig. 4 with those extracted from the Fourier transforms of  $C(t)$ . We observe quantitative agreement on the attractive side, while at unitarity and for strong repulsive

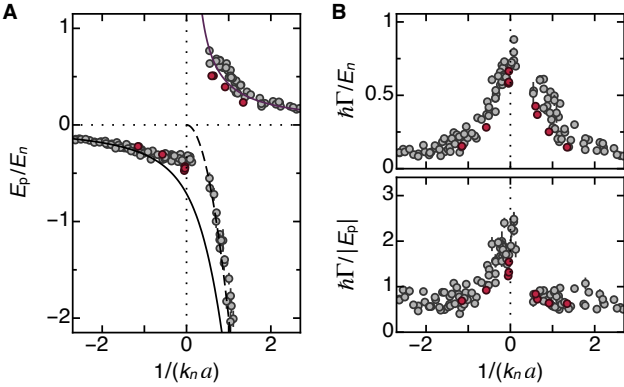


FIG. S8. Comparison of extracted quantities from spectroscopy and interferometry. We reproduce panels from Fig. 4, showing the spectroscopy data for  $B_{\text{res}} = 526.2\text{G}$  (gray points). The red points show  $E_p$  and  $\Gamma$  extracted from the Fourier transforms of  $C(t)$  (see *e.g.* Fig. 2D).

interactions we observe small systematic differences. Note that the differences in  $E_p$  are a small fraction of  $\Gamma$  (see also Fig. 2).